Surfaces and Interfaces 35 (2022) 102440

Contents lists available at ScienceDirect

Surfaces and Interfaces

journal homepage: www.sciencedirect.com/journal/surfaces-and-interfaces

One-step method to prepare coccinellaseptempunctate-like silver nanoparticles for high sensitivity SERS detection

Siyu Wang [a,b,d], Shichuan Xi [a,b], Ruhao Pan [c], Yang Yang [c], Zhendong Luan [a,b], Jun Yan [a,b], Xin Zhang [a,b,d,*]

[a] Key Laboratory of Marine Geology and Environment & Center of Deep Sea Research, Institute of Oceanology, Center for Ocean Mega-Science, Chinese Academy of Sciences, Qingdao 266071, China
[b] Laboratory for Marine Geology, Pilot Laboratory for Marine Science and Technology (Qingdao), Qingdao 266061, China
[c] Beijing National Laboratory for Condensed Matter Physics, Institute of Physics, Chinese Academy of Sciences, Beijing 100190, China
[d] University of Chinese Academy of Sciences, Beijing 101408, China

ARTICLE INFO

Keywords:
Annealing process
Surface-enhanced Raman spectrometry
Phosphoethanolamine
High-pressure
Deep-sea

ABSTRACT

The surface morphology of metal particles can be adjusted by the annealing process to enhance the activity of Raman substrate and achieve an ultra-low concentration detection limitation. In this study, a surface-enhanced Raman scattering (SERS) substrate of coccinellaseptempunctate-like silver nanospheres coated with a silver nanoisland structure (Ag NI@Ag NSs) was prepared using a simple annealing process. Numerous silver nanospheres were dispersed on the surface of the silver nanoislands, which exhibited a single crystal plane (111) orientation. The SERS substrate had an enhancement factor of 10^8 for Rhodamine B (Rh B) and was highly sensitive to phosphoethanolamine (PETA). The SERS response toward PETA showed excellent correlation during the range of 5×10^{-7} - 1×10^{-5} mol/L with the detection limitation as low as 5×10^{-7} mol/L, and the correlation coefficient is 0.9918. The simulated high-pressure test showed that the SERS response could be still observed at 1100 m sub ocean pressure even with a PETA concentration of 1 mM. The test results of selectivity, reproducibility, and accuracy indicated that the Ag NI@Ag NS sensor possessed potential applications in the deep-sea analytical and other related fields.

1. Introduction

In-situ deep-sea exploration presents great challenges because of the extreme and complex deep-sea environment (cold seeps and hydrothermal vents). Raman spectroscopy has the advantages of non-contact, direct detection, and simultaneous detection of multiple components, therefore, it has been widely used in *in-situ* deep-sea detection [1]. Sheri et al. employed the deep ocean Raman *in-situ* spectrometer (DORISS) system for the *in-situ* detection of deep-sea hydrothermal vent fluids and successfully obtained the *in-situ* Raman spectra of high-temperature hydrothermal fluids at a depth of approximately 2700 m [1,2]. Zhang et al. developed a deep-sea Raman insertion probe system [3], which realized *in situ* detection and analysis of physicochemical parameters of high-temperature (up to 450 °C) hydrothermal vent fluid temperature, composition (such as CO_2, SO_4^{2-}/HSO_4^-, and H_2.) [4], minerals [5], and overlying biota falling water [6]. These *in-situ* data evidenced that the deep-sea fluid content is much higher than the previous reports, indicating the importance of the *in-situ* data acquisition.

The symbiotic mechanism between metazoans and chemoautotrophs is an important factor in maintaining the stability and sustainable life activities of deep-sea ecosystems, and it has become a point of discussion in deep-sea research [7,8]. Anaerobic oxidation of methane (AOM) mediated by Anaerobic Methanotrophic Archaea (ANME) is the primary process that provides energy to cold seep ecosystems by converting methane into inorganic carbon. The AOM process attenuates the emission of the greenhouse gas methane and supports a large, diverse microbial, and animal population [9–12]. Meanwhile, the head group of phosphatidylethanolamines (PE) can be used as a biomarker for archaeal symbiotic bacteria [13]. Moreover, the formation of the head group of PE is related to the formation of phosphoethanolamine (PETA) [14]. Therefore, the trace detection of PETA is of great significance for identifying the presence of deep-sea symbiotic bacteria and *in-situ*

* Corresponding author at: Key Laboratory of Marine Geology and Environment & Center of Deep Sea Research, Institute of Oceanology, Center for Ocean Mega-Science, Chinese Academy of Sciences, Qingdao 266071, China.
E-mail address: xzhang@qdio.ac.cn (X. Zhang).

https://doi.org/10.1016/j.surfin.2022.102440
Received 8 September 2022; Accepted 22 October 2022
Available online 24 October 2022

detection of symbiotic bacterial metabolites. However, there is rare *in-situ* detection technologies for deep-sea extracellular metabolism. Traditional detection methods, such as colorimetry, liquid chromatography-coupled mass spectrometry (LC-MS), and nuclear magnetic resonance (NMR), cannot detect multicomponent simultaneously, are time-consuming, expensive and have a low sensitivity [15–17]. Meanwhile, owing to the detection limitation of the Raman spectrum, it is difficult to detect deep-sea microbial metabolites or intermediates at low concentrations.

Surface-enhanced Raman scattering (SERS) mainly originates from the enhancement of the local electromagnetic field close to the precious metals (Ag and Au); therefore, it has the ability of ultrasensitive and rapid detection of trace molecules [18–21]. At present, the commonly used Raman signal enhancement media mainly include SERS substrates and nanosol. A SERS substrate is necessary to meet the requirements of deep-sea *in situ* experiments. Metal nanostructures dispersed on the sub-nanometer gap substrates are ideal for enhancing SERS signals [22]. Because the scattering cross-section of Ag is larger than that of Au, Ag is more advantageous than Au in the visible region [23]. The size [24,25], shape [26,27], and exposure surface of the metal nanostructures [28] are important factors for achieving chemical enhancement. Studies have shown that the Ag (111) facet had the lowest free energy; particularly, the Ag (111) facet had a stronger ability to adsorb molecules than other crystal surfaces, thus increasing the chemical enhancement of SERS [29, 30]. In summary, it is necessary to design SERS substrates that can adsorb various of molecules at a low cost and with high stability, and oxidation resistance.

From this perspective, we used a high-temperature annealing process to treat the quartz of the silver coated film and annealed it in air atmosphere to obtain silver nanospheres (Ag NSs) loaded with a silver nanoisland (Ag NI) structure. Many nanospheres were dispersed on each nanoisland, with a diameter of approximately 40 nm and a spacing ranging from 5 to 70 nm, which had an excellent SERS effect. Considering that the pressure at deep-sea cold seeps is greater than 11 MPa, the SERS substrate should have high oxidation resistance and be detected under ultra-high pressure. As a proof of concept, we simulated PETA (cell concentration levels, 1 mM) at the Ag NI@Ag NSs substrate under cold seeps pressure for detection.

2. Materials and methods

2.1. Materials

The Ag nanofilm/quartz was provided by the Instituteis of Physics, Chinese Academy of Sciences. Phosphoethanolamine (PETA, ≥98.0%), L-threonine (≥98.0%), L-tryptophan (≥98.0%), rhodamine B (Rh B), 3-phenyl-L-alanine (≥98.0%) and anhydrous ethanol were purchased from Sigma-Aldrich. Ultrapure water (18.2 MΩ cm, produced by a Milli-Q system) was used in this study.

2.2. Preparation of silver nanofilm/quartz substrate

The clean quartz substrate was loaded into the chamber of an electron beam deposition system (EBD FU-12PEB), and then the Ag film was deposited on the substrate at a rate of 2 A/s. A thickness monitor was introduced to measure the film thickness, and a silver film with a thickness of 100 nm was obtained after the EBD process.

2.3. Annealing process fabricate Ag NI@Ag NSs/quartz

The Ag nanofilm/quartz substrate was then annealed in a muffle furnace. The heating rate for the annealing process was 10°C/s. The substrate was heated up to 420°C and held for 10 min in air before cooling to 20°C. During the annealing process of Ag film/quartz, accurate temperature control is significant. Additionally, to ensure the growth of uniformly dispersed Ag nanoparticles on the Ag nanoisland under similar experimental conditions, substrates at 300, 340, 380 and 440°C were prepared by changing the annealing temperature.

2.4. Surface enhanced Raman scattering measurement

First, Ag NI@Ag NSs on quartz were cleaned ultrasonically in acetone, ethanol, and deionized water and then stood or blow-dried with nitrogen for later use. The device used for the SERS was a confocal Raman microscope (WITec Alpha300 R System) produced by the German WITec Company [31]. All sample spectra were collected using controlled FIVE software processed using Project FIVE 5.0 and GRAMS/AI 9.3 software for smooth baseline calibration and peak fitting. Gaussian fitting was used to obtain the Raman shift, peak width, and peak area of the three Raman peaks. The excitation laser wavelength was 532 nm, and the HE-NE laser microscope lens were ZEISS EC Epiplan 100x/0.9 and ZEISS EC Epiplan 61x/1.0 water immersion objective lens. The lens could control the laser spot size to 0.9 micron while providing a clear microstructure of the sample; the laser power was 5 mW. Each SERS was accumulated 20 times during the measurement process, and the integration time was set to 1 s. The signal-to-noise ratio of the obtained spectrum was high. The characteristic Raman peak Si (520 cm^{-1}) was used to calibrate the spectrometer PETA.

2.5. Simulation methods

The electric field distribution of the Ag NI@Ag NSs was simulated the finite difference time domain (FDTD) method. The radius of the Ag NI and Ag nanospheres was 400 nm, and 20 nm, respectively, and the gap between the spheres was approximately 5 nm and 70 nm. The incident light was set to a wavelength of 532 nm and propagated along the z-axis, with the electric field polarized along the x-axis. Here, three monitors were placed perpendicular to the x, y, and z axes to capture the field distribution fully. The entire simulation region was set to 900 × 900 × 900 nm, and all the boundaries were perfectly matched layer boundary conditions. The simulation time was set to 500 FS to ensure complete attenuation of the energy field. The mesh size is 1.5 × 1.5 × 2 nm.

3. Result and discussion

3.1. Synthesis process of Ag NI@Ag NSs and SERS enhanced mechanism

In this study, high-temperature annealing process was used to prepare coccinellaseptempunctate-like silver nanoparticles SERS substrate. The main technological processes is shown in Fig. 1a. First, a quartz plate was deposited on a 100 nm thick silver film and then subjected to thermal annealing treatment in an air atmosphere. A porous Ag film can be obtained by thermal annealing at approximately 300 °C (corresponding to Fig. S1a). When the annealing temperature was changed between 320 and 380 °C, the silver film melted at high temperatures to form a smooth nanoisland structure with uniform dispersion (corresponding to Fig. S1b–d). A very distinct morphology was formed at 420 °C. The previously obtained nanoisland gradually became disordered, and many silver nanoparticles grew on the nanoisland surface, similar to the back pattern of the coccinellaseptempunctate. We refer to this as the Ag NI@Ag NSs (corresponding to Fig. S1e). The enhancement mechanism of the Ag NI@Ag NSs is shown in Fig. 1b. As Ag (111) crystal planes dominate Ag nanoparticles, the low free energy leads to a strong adsorption capacity; therefor, the measured molecules can be easily adsorbed on the surface of Ag NI@Ag NSs. Furthermore, the spacing of the silver nanoparticles on the surface of the silver nanoisland was between 5 and 70 nm (Fig. S2e) and strong surface plasmon resonance enhanced Raman signal. The synergistic effect of chemical enhancement mechanism (CM) and electromagnetic enhancement mechanism (EM) resulted in excellent SERS activity of the Ag NI@Ag NSs.

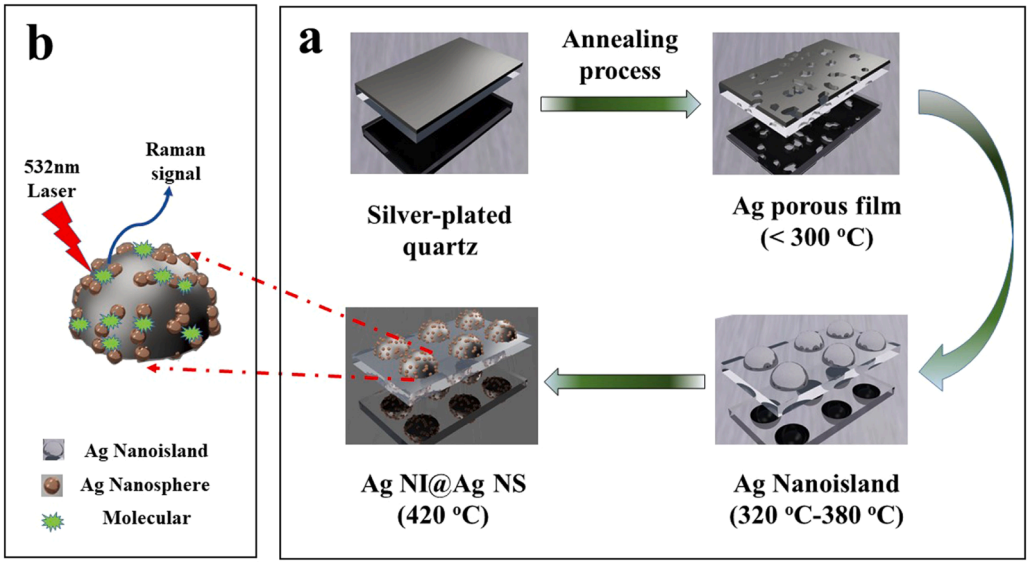

Fig. 1. Schematic of fabrication process of Ag NI@Ag NSs (a); and SERS enhancement mechanism (b).

3.2. Morphology and structure analysis

Fig. 2A shows a scanning electron microscope (SEM) image of the as-prepared silver film after high-temperature annealing for 10 min at 380 °C, showing a smooth and evenly dispersed granular structure with an average size of approximately 800 nm. The single crystal morphology (Fig. 2B) also proved that its surface was very smooth. However, irregularly shaped silver nanoislands were formed when we set the temperature to 420 °C (Fig. 2C). Further enlarged image of a single nanoisland (Fig. 2D) showed many smaller nanoparticles of approximately 20 nm in size on the surface of the nanoisland, which was similar to the decorative pattern of coccinellaseptempunctates. The morphological and structural evolution of the silver film were studied by varying the reaction temperature (Figs. S1, S2), which supports our hypothesis (in the *Supporting Information)*.

Energy Dispersive X-Ray Spectroscopy (EDX) elemental mapping obtained from the surface proved the elemental composition of the nanoparticles on the surface of the silver nanoislands. As shown in Fig. 3a, there are no oxygen atoms on the silver nanoisland; thus, the tiny nanoparticles loaded on its surface are all Ag nanoparticles. As the substrate was annealed in an aerobic environment of 320 °C, the Ag nanoparticles were still not oxidized, indicating that the Ag NI@Ag NS substrate has excellent oxidation resistance, which laid a foundation for its application in complex deep-sea environments. XRD (Fig. 3b) showed that the Ag base exposed only the Ag (111) crystal facet. Additionally, from the HRTEM image of Ag NI@Ag NSs, the calculated "d" spacing was 0.23 nm, which matched the most intense reflection from the (111) facet corresponding the fcc structure of Ag nanoparticles [32,33], and only the lattice fringe of Ag (111) was observed (Figs. 3c, d and S5). Among all the planes, the (111) facet had the lowest free energy. Thus, the (111) facet could adsorb molecules more strongly than the other surfaces, increasing the chemical enhancement of SERS [29]. And then, because the substrate was annealed in an air atmosphere, its oxidation resistance was improved [25].

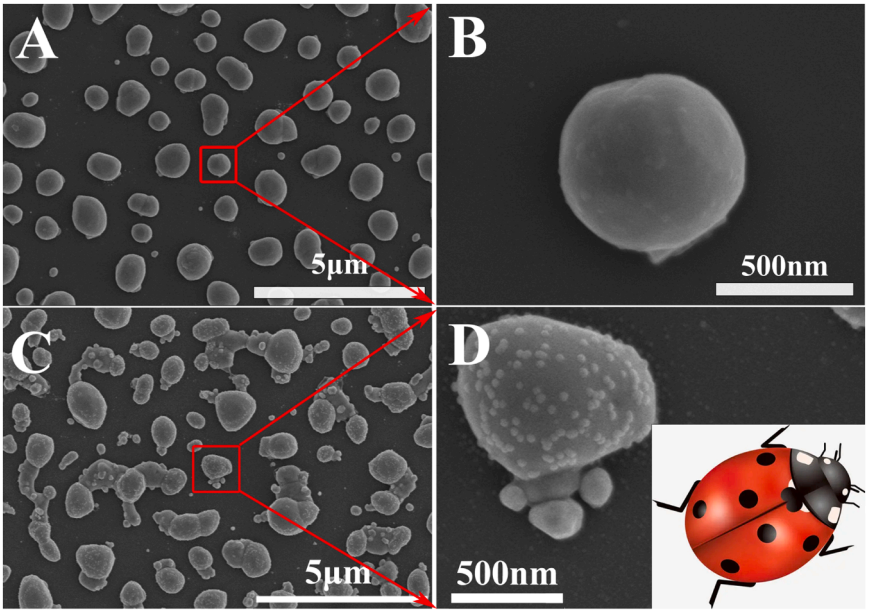

Fig. 2. The SEM of (A), (B) Ag NS (380 °C) and (C), (D) AgNI@AgNSs.

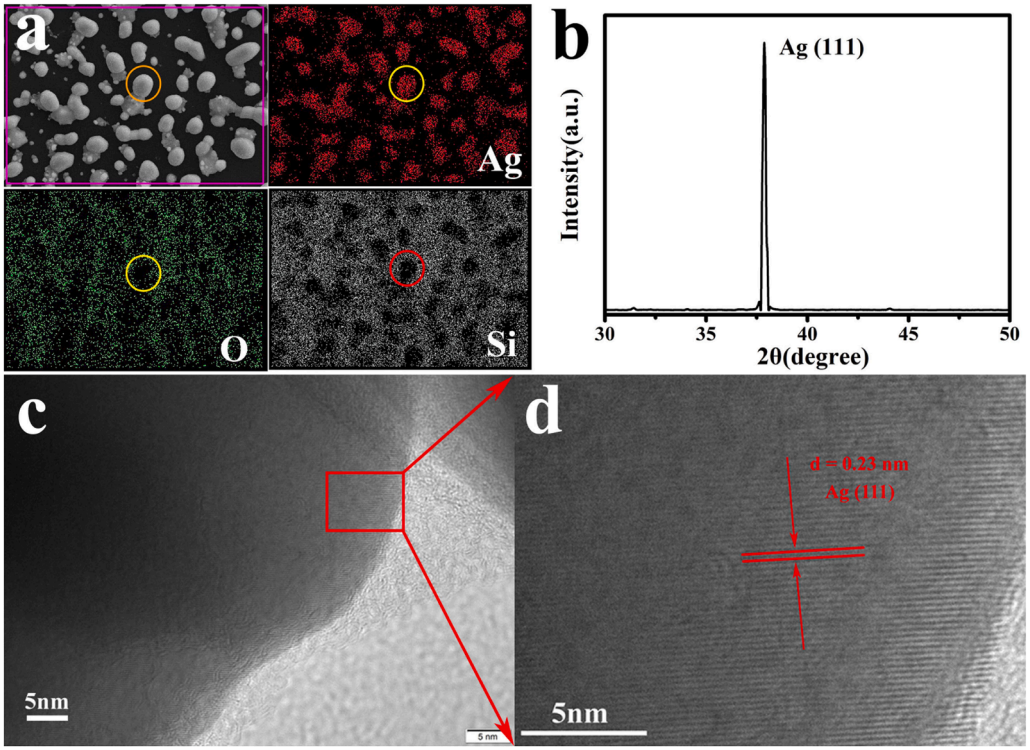

Fig. 3. The (a) Mapping image, (b) XRD, (c, d) HRTEM image of AgNI@AgNSs.

3.3. Electromagnetic field distribution: FDTD simulation

To investigate the origin of the SERS enhancement of Ag NI@Ag NSs observed in the experiment, we performed FDTD simulations of silver nanoislands and silver nanospheres grown on a quartz substrate. Fig. 4 shows the x-z view electric field distribution of the coupled nanostructure at an excitation wavelength of 532 nm. A large field enhancement occurs at the junction of the silver nanoislands and silver nanospheres. Therefore, the large field intensity generated by the local surface plasmon coupling of silver nanoislands and silver nanospheres can induce the SERS enhancement of the Ag NI@Ag NSs. In addition, a large field enhancement was observed between silver nanospheres. The silver nanospheres on the inclined plane have a higher pair field strength and more hot spots. Thus, nanoscale gaps between the metal nanostructures are the main source of Raman scattering enhancement [34, 35]. EF is usually defined as $(E/E_0)^4$, where E is the local maximum electric field, and E_0 is the amplitude of the input source electric field in a linear simulation [36]. A large field enhancement (2.56×10^6) is observed at the junction between the nanostructures (Fig. S3). The discrepancy in the calculated EF between the experimental and FDTD simulations was that (I) SERS enhancement was a combined effect of EM enhancement and chemical enhancement, although only the EM enhancement was considered in the FDTD simulation; (II) the size and shape of the silver nanoislands were different, and the size and distance of silver nanospheres distributed on the silver nanoislands were different, which is shown in the SEM image in Fig. 2D. This variation in size and distance between them affects the incoming EM radiation. However, in the FDTD simulation, only the effects of silver nanoislands and nanospheres were considered in the ideal state.

3.4. Measurement of SERS activity

Herein, an as-fabricated sample of coccinellaseptempunctate-like silver nanoparticles (Ag NI@Ag NSs) was used as a SERS probe, and Rhodamine B (Rh B) was used as a Raman probe to measure the SERS enhancement in Ag NI@Ag NSs. Different substrates calcined at 340, 380, 420, and 440 °C were immersed for 2 h in Rh B solution with 10^{-6} M concentration to obtain the optimal SERS substrate with the highest sensitivity, and Raman spectra are obtained after drying, as shown in Fig. 5a. There was no obvious correlation between the strength and

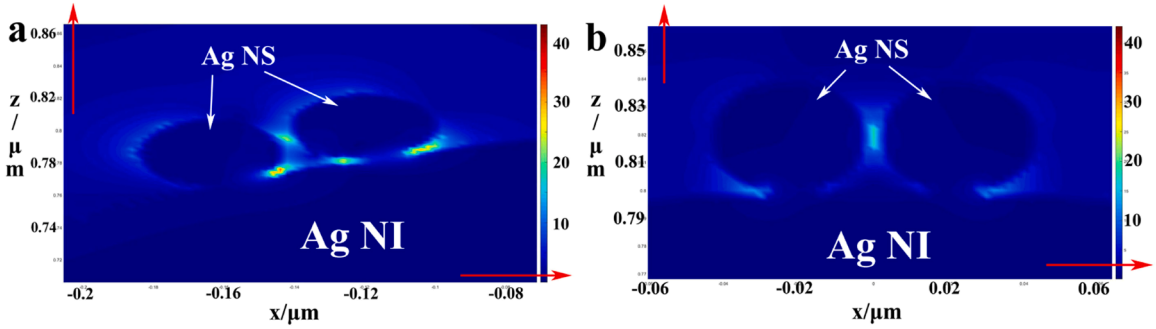

Fig. 4. The finite difference time domain (FDTD) method is used to calculate the electric field distribution of the combination of Ag nanoisland and Ag nanosphere on the quartz substrate under the excitation of 532 nm: (a) and (b).

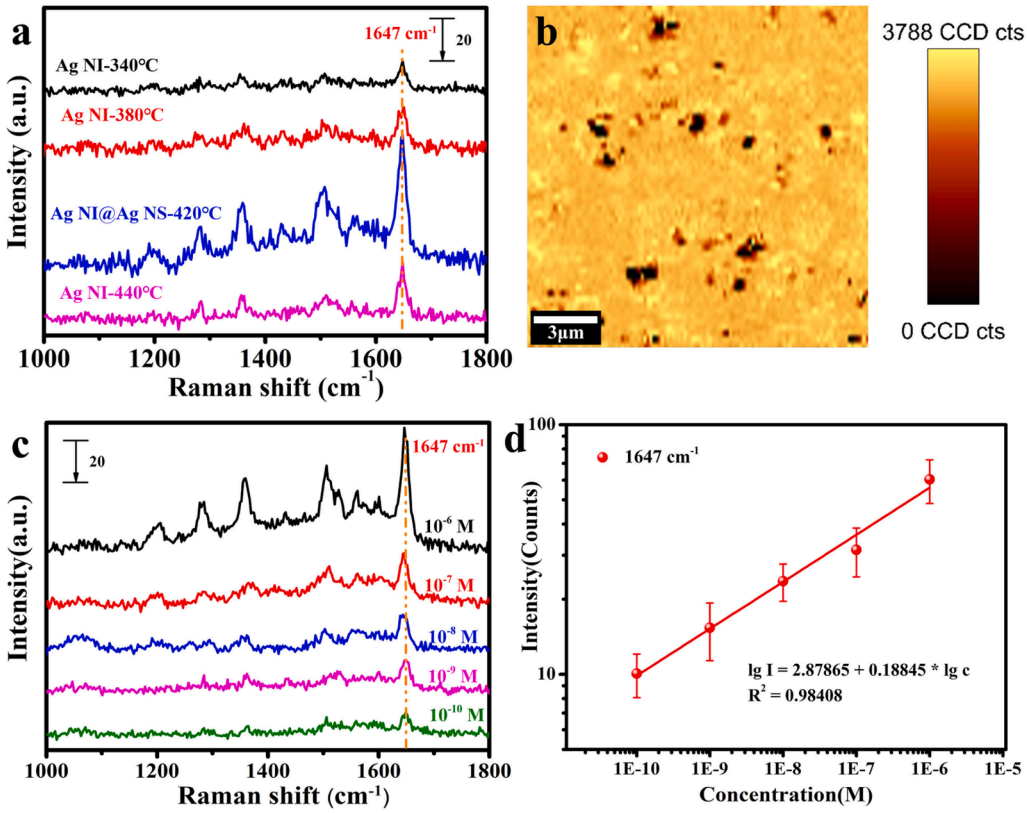

Fig. 5. (a) SERS spectra of Rhodamine B (Rh B) (10^{-6} M) with different temperature Annealing process in the range of 340 °C to 440 °C, and the immersion time was the same. (b) Raman mapping (15 μm × 15 μm) of the SERS substrate treated with the 1 × 10^{-6} M Rh B solution (the peak, 1647 cm $^{-1}$). (c) SERS spectra of Rh B with different concentrations in the range of 10^{-6} M to 10^{-10} M, and the immersion time was the same. (d) The intensity of the Raman characteristic peak of Rh B at 1647cm^{-1} varies from 10^{-6} to 10^{-10} M (on a logarithmic scale) as a function of molecular concentration, corresponding to (c).

calcination temperature. When the temperature was 420 °C, the Raman strength was the highest, that is, the sensitivity was the highest. This proved that the formation of coccinellaseptempunctate-like silver nanoparticle (Ag NI@Ag NSs) structures improved the SERS sensitivity. The 1647 cm^{-1} band was selected as the analytical marker, as this band intensity was more sensitive to RhB concentration with lower background noise [37]. Raman mapping was performed on the surface of the Ag NI@Ag NS substrate (15 μm × 15 μm), and we measured 120 × 60 points in the SERS substrate (Fig. 5b). The matrix was also treated with 1 × 10^{-6} M Rh B solution. Raman mapping is based on the spectral intensity at a given wave number, showing regions of different colors according to the peak intensity of Rh B at 1647 cm^{-1}. In Fig. 5b, the locations of the bright yellow area have the strongest SERS performance, whereas the locations of the black area have a relatively low SERS performance. The bright yellow areas are evenly distributed, occupying most space as shown in Fig. 5b. Raman mapping revealed the good reproducibility of the Ag NI@Ag NS substrates from a microscopic point of view. We successively obtained the Raman spectra of Rh B molecules at a concentration in the range of 10^{-6} M to 10^{-10} M on Ag NI@Ag NSs to determine the sensitivity of Ag NI@Ag NSs as SERS probes, as shown in Fig. 5c. The results show that the Ag NI@Ag NS substrate has a good response to 10^{-10} M Rh B. Fig. 5d shows the linear relationship between intensity and concentration of typical Rh B characteristic peak at 1647 cm^{-1}. The curve equation is lg I = 2.879 + 0.18845 × (lg c), and the correlation coefficient is 0.9841.

To measure the enhancement of the Raman signal of Rh B, the following formula was used [44]:

$$EF = [(I_{SERS}) / (I_{Normal})] \times [(N_{Normal}) / (N_{SERS})]. \quad (1)$$

The calculated results indicated that the SERS EF of Rh B in the Ag NI@Ag NSs structure can be estimated to be 10^8 (in the *Supporting Information*). Table 1 compares the SERS EF reported in the literature and our work on Ag NI@Ag NSs.

Table 1
Comparison of SERS EF between different samples with our work of Ag NI@Ag NS.

Sample	Dye	SERS EF	Refs.
Ag thin film	Crystal violet	5.3 × 10^5	[38]
Ag NP on TO-Nanopaper	Rh B	1.46 × 10^9	[37]
Cabbagelike (111) Faceted Ag Crystals	Rhodamine 6G	3.5 × 10^6	[30]
Ag NP on PDMS	Rhodamine 6G	10^9	[39]
Ag NP on planar Si	Rhodamine 6G	10^8	[25]
Ag/PDA/ZnO@GMF	Rh B	10^{10}	[40]
Ag@AAO DHPCs	Rh B	1.3 × 10^6	[41]
ZnO-NC/Au/Ag_{152}	Rh B	6.48 × 10^9	[42]
Ag NPs/filter paper	Rhodamine 6G	1.42 × 10^{10}	[43]
Ag NI@Ag NSs	Rh B	10^8	This work

3.5. Properties and identification mechanisms of Ag NI@Ag NSs for PETA

A 10^{-5} M aqueous solution of PETA was chosen as the target molecule to estimate the SERS activity of Ag NI@Ag NSs for biomolecules. The SERS spectra of the pure PETA crystal on a quartz plate were collected for comparison (Fig. S8, in the *Supporting Information*), and the main vibration of PETA was confirmed according to the reported study. As shown in Fig. 6a, the Raman strength gradually increased with the increase of PETA concentration due to its specific adsorption more PETA molecular lines specifically adsorbed onto the recognition sites of Ag NI@Ag NSs. The relationship between peak intensity at 935 cm^{-1} and PETA concentration was plotted, and the linear relationship between Raman intensity (I) and logarithm (c) of PETA concentration in the range of 5 × 10^{-7} - 1 × 10^{-5} mol/L was obtained (Fig. 6b). The curve equation is I = 148.12 + 20.96 × (lg c), and the correlation coefficient is 0.9918. To further verify the adsorption mechanism of PETA onto by Ag

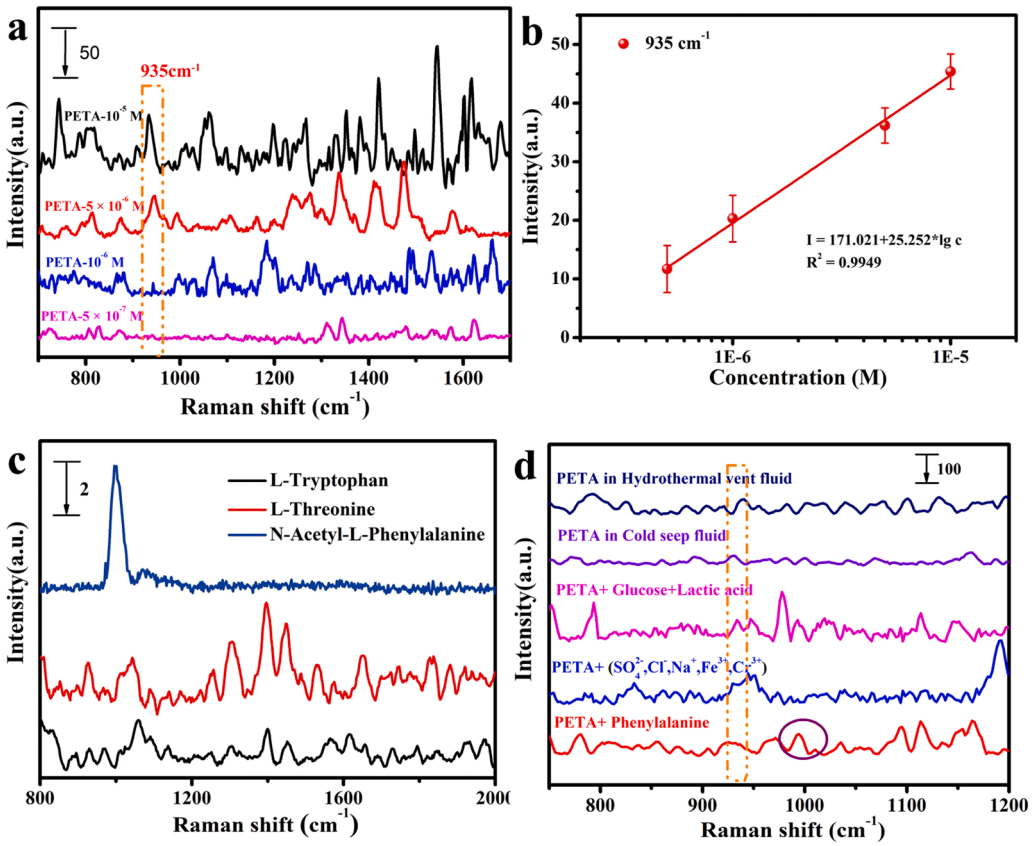

Fig. 6. (a) SERS spectra of phosphoethanolamine on Ag NI@Ag NSs; (b) Calibration curve of phosphoethanolamine; (c) Comparison of SERS spectra of L-tryptophan, L-threonine and N-acetyl-L-phenylalanine based on Ag NI@Ag NSs (1×10^{-6} M); (d) Typical SERS spectra of phosphoethanolamine (10^{-6} mol/L) and interfering substances.

NI@Ag NSs, the SERS spectra of three other types of amino acids was collected. As shown in Fig. 6c, the main characteristic peaks of amino acids (*1051 cm^{-1} (CO, OH) and 1070 cm^{-1} (CN)*) could be observed and it was therefore proposed that the mechanism of chemical enhancement was mainly caused by the chemical adsorption of Ag-N bond [45].

Recognition specificity is an important index for sensors. To test the selectivity of the Ag NI@Ag NSs sensor in complex environmental samples, several components in deep-sea fluids, including cations, anions, metabolites, amino acids, and deep-sea *in-situ* samples (hydrothermal vent fluids and cold seep fluids) have been selected as interfering substances and used in conjunction with PETA. Compared with the concentration of PETA, more than 5 times the concentration of interference substances were introduced into the solution. As shown in Fig. 6d, these interfering substances and blank samples caused almost equal intensities on Raman signals response at 935 cm^{-1}. These results demonstrated the excellent selectivity of this sensor, and it was suitable to be utilized in complex systems. Meanwhile, in the mixture of PETA and phenylalanine, the characteristic peak of PETA (935 cm^{-1}) and the characteristic peak of phenylalanine (1004 cm^{-1}) were detected simultaneously (Fig. 6d, red curve). It could be further proved that the recognition mechanism of PETA and amino acids by the substrate was due to the chemisorption of Ag-N bond.

3.6. Application of the Ag NI@Ag NSs sensor in the simulated environment

The feasibility of actual deep-sea detection was explored using standard seawater (China Series Standard Seawater *(GBW(E) 130011), Salinity 40.004*, was purchased from were purchased from *Standard Information Network*) as the solvent to prepare 1 mM PETA solution and adjusting the pH ≈ 7.9 (simulating the pH at a cold seep. A ZEISS EC Epiplan 61x/1.0 water immersion objective lens was used. The effect of high pressure on SERS performance was explored using a *micro-visualized low-temperature high-pressure reaction chamber* (Fig. S6) to conduct a cold-seep high-pressure simulation experiment. The pressure was set at 5, 8, and 11 MPa, and the PETA concentration was 1 mM (considering the attenuation of the Raman signal after passing through the sapphire window and the content of PETA in biological cells reported in some papers). The pressure-dependent SERS spectra were measured under 532 nm laser excitation. The results are shown in Fig. 7a, b. Under high pressure, there was still a good SERS effect; the characteristic peak of the target became increasingly obvious with the increase in pressure. This was because the increase in pressure led to a decrease in the distance between the molecules to be measured and the SERS base, thereby increasing the SERS enhancement effect. Raman mapping was performed on the Ag NI@Ag NSs substrate (150 μm × 150 μm, 120 × 60 points) for 1 mM PETA at 11 MPa (Fig. S7), showing regions of different colors according to the peak intensity of at 935 cm^{-1}. Raman mapping revealed good reproducibility at high pressures from a microscopic perspective. The success of the solution environment simulation experiment further confirms the feasibility of SERS detection in the deep sea.

4. Conclusions

In conclusion, a coccinellaseptempunctate-like (silver nanospheres coated with silver nanoisland structures, Ag NI@Ag NSs) SERS substrate was prepared using a simple annealing process. Researches show that the nanogaps between the nanosphere and the nanoisland are the main distribution area of “hot spots”. The SERS substrate showed excellent crystal orientation, which significantly increased the chemical enhancement of the substrate. Using Rh B as the signal molecule, we tested an enhancement factor of 10^8. Furthermore, the Ag NI@Ag NSs

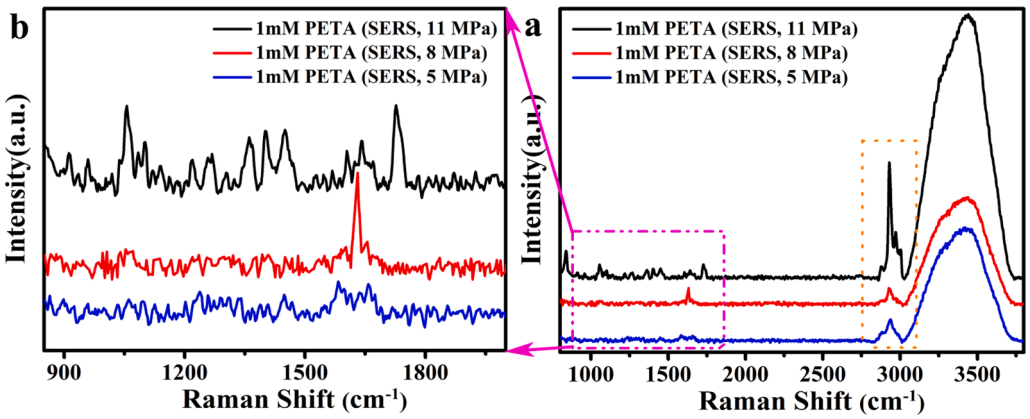

Fig. 7. (a, b) Simulated cold seeps pressure test (1 mM PETA, the pressures are 5, 8 and 11 MPa).

showed good selectivity, reproducibility, accuracy, and the target molecule PETA was detected at 11 MPa. The SERS substrate has been processed with high-temperature annealing and has strong oxidation resistance, which can overcome the difficulty of pressure in cold seeps, providing a basis for deep-sea *in situ* detection.

To the best of our knowledge, this is the first study on silver nanospheres coated with a silver nanoisland morphology by adjusting the annealing temperature of noble metal nanoparticles. Single crystal-oriented noble metal nanoparticles were obtained to realize SERS enhancement. Although the prepared substrate had excellent EM and CM effects, the SERS effect was limited owing to the great difference in morphology and large spacing between nanoislands. This provides ideas for further improvement.

CRediT authorship contribution statement

Siyu Wang: Conceptualization, Methodology, Data curation, Writing – original draft. **Shichuan Xi:** Software, Resources, Formal analysis. **Ruhao Pan:** Resources, Formal analysis. **Yang Yang:** Funding acquisition, Project administration. **Zhendong Luan:** Funding acquisition, Project administration, Supervision. **Jun Yan:** Funding acquisition, Project administration. **Xin Zhang:** Funding acquisition, Project administration, Supervision, Writing – review & editing.

Declaration of Competing Interest

The authors declare that there are no conflicts of interest.

Data availability

No data was used for the research described in the article.

Acknowledgments

This research was supported by the following grants: the Strategic Priority Research Program of Chinese Academy of Sciences (XDA22050100); the National Natural Science Foundation of China (92058206); the Senior User Project of ROV KEXUE (KEXUE2019GZ06), Key project of Ocean Research Center, Chinese Academy of Sciences (COMS2020J03); the Young Taishan Scholars Program (tsqn201909158); Natural Science Foundation of Shandong Province (ZR2019BD029); The China Postdoctoral Science Foundation (2020M682245). This work was supported by the Synergetic Extreme Condition User Facility (SECUF).

References

[1] P.G. Brewer, G. Malby, J.D. Pasteris, S.N. White, E.T. Peltzer, B. Wopenka, J. Freeman, M.O. Brown, Development of a laser Raman spectrometer for deep-ocean science, Deep Sea Res. Part I Oceanogr. Res. Pap. 51 (2004) 739–753, https://doi.org/10.1016/j.dsr.2003.11.005.

[2] S.N. White, R.M. Dunk, E.T. Peltzer, J.J. Freeman, P.G. Brewer, *In situ* Raman analyses of deep-sea hydrothermal and cold seep systems (Gorda Ridge and Hydrate Ridge), Geochem. Geophys. Geosyst. 7 (2006), https://doi.org/10.1029/2005GC001204.

[3] X. Zhang, P.M. Walz, W.J. Kirkwood, K.C. Hester, W. Ussler, E.T. Peltzer, P. G. Brewer, Development and deployment of a deep-sea Raman probe for measurement of pore water geochemistry, Deep Sea Res. Part I Oceanogr. Res. Pap. 57 (2010) 297–306, https://doi.org/10.1016/j.dsr.2009.11.004.

[4] L. Li, X. Zhang, Z. Luan, Z. Du, S. Xi, B. Wang, L. Cao, C. Lian, J. Yan, *In situ* quantitative raman detection of dissolved carbon dioxide and sulfate in deep-sea high-temperature hydrothermal vent fluids, Geochem. Geophys. Geosyst. 19 (2018) 1809–1823, https://doi.org/10.1029/2018GC007445.

[5] S. Xi, X. Zhang, Z. Du, L. Li, B. Wang, Z. Luan, C. Lian, J. Yan, Laser Raman detection of authigenic carbonates from cold seeps at the Formosa Ridge and east of the Pear River Mouth Basin in the South China Sea, J. Asian Earth Sci. 168 (2018) 207–224, https://doi.org/10.1016/j.jseaes.2018.01.023.

[6] X. Zhang, K.C. Hester, W. Ussler, P.M. Walz, E.T. Peltzer, P.G. Brewer, *In situ* Raman-based measurements of high dissolved methane concentrations in hydrate-rich ocean sediments, Geophys. Res. Lett. 38 (2011), https://doi.org/10.1029/2011GL047141.

[7] J.J. Childress, P.R. Girguis, The metabolic demands of endosymbiotic chemoautotrophic metabolism on host physiological capacities, J. Exp. Biol. 214 (2011) 312–325, https://doi.org/10.1242/jeb.049023.

[8] A.L. Reysenbach, Y. Liu, A.B. Banta, T.J. Beveridge, J.D. Kirshtein, S. Schouten, M. K. Tivey, K.L. Von Damm, M.A. Voytek, A ubiquitous thermoacidophilic archaeon from deep-sea hydrothermal vents, Nature 442 (2006) 444–447, https://doi.org/10.1038/nature04921.

[9] S. Yang, Y. Lv, X. Liu, Y. Wang, Q. Fan, Z. Yang, N. Boon, F. Wang, X. Xiao, Y. Zhang, Genomic and enzymatic evidence of acetogenesis by anaerobic methanotrophic archaea, Nat. Commun. 11 (2020) 3941, https://doi.org/10.1038/s41467-020-17860-8.

[10] C.J. Hahn, R. Laso-Pérez, F. Vulcano, K.M. Vaziourakis, R. Stokke, I.H. Steen, A. Teske, A. Boetius, M. Liebeke, R. Amann, K. Knittel, G. Wegener, Candidatus Ethanoperedens," a thermophilic genus of archaea mediating the anaerobic oxidation of ethane, mBio 11 (2020) e00600–e00620, https://doi.org/10.1128/mBio.00600-20.

[11] K.W. Seitz, N. Dombrowski, L. Eme, A. Spang, J. Lombard, J.R. Sieber, A.P. Teske, T.J.G. Ettema, B.J. Baker, Asgard archaea capable of anaerobic hydrocarbon cycling, Nat. Commun. 10 (2019) 1822, https://doi.org/10.1038/s41467-019-09364-x.

[12] S.C. Chen, N. Musat, O.J. Lechtenfeld, H. Paschke, M. Schmidt, N. Said, D. Popp, F. Calabrese, H. Stryhanyuk, U. Jaekel, Y.G. Zhu, S.B. Joye, H.H. Richnow, F. Widdel, F. Musat, Anaerobic oxidation of ethane by archaea from a marine hydrocarbon seep, Nature 568 (2019) 108–111, https://doi.org/10.1038/s41586-019-1063-0.

[13] M.Y. Kellermann, F. Schubotz, M. Elvert, J.S. Lipp, D. Birgel, X. Prieto-Mollar, N. Dubilier, K.U. Hinrichs, Symbiont–host relationships in chemosynthetic mussels: A comprehensive lipid biomarker study, Org. Geochem. 43 (2012) 112–124, https://doi.org/10.1016/j.orggeochem.2011.10.005.

[14] H.A. Boumann, E.C. Hopmans, I. Van De Leemput, H.J.M. Op den Camp, J. Van De Vossenberg, M. Strous, M.S.M. Jetten, J.S. Sinninghe Damsté, S. Schouten, Ladderane phospholipids in anammox bacteria comprise phosphocholine and phosphoethanolamine headgroups, FEMS Microbiol. Lett. 258 (2006) 297–304, https://doi.org/10.1111/j.1574-6968.2006.00233.

[15] S. Yong, S. Lau, Rapid separation of tryptophan, kynurenines, and indoles using reversed-phase high-performance liquid chromatography, J. Chromatogr. A 175 (1979) 343–346, https://doi.org/10.1016/S0021-9673(00)89443-1.
[16] J.L. Markley, R. Brüschweiler, A.S. Edison, H.R. Eghbalnia, R. Powers, D. Raftery, D.S. Wishart, The future of NMR-based metabolomics, Curr. Opin. Biotechnol. 43 (2017) 34–40, https://doi.org/10.1016/j.copbio.2016.08.001.
[17] J. Plou, I. García, M. Charconnet, I. Astobiza, C. García-Astrain, C. Matricardi, A. Mihi, A. Carracedo, L.M. Liz-Marzán, Multiplex SERS detection of metabolic alterations in tumor extracellular media, Adv. Funct. Mater. 30 (2020), 1910335, https://doi.org/10.1002/adfm.201910335.
[18] S.Y. Ding, E.M. You, Z.Q. Tian, M. Moskovits, Electromagnetic theories of surface-enhanced Raman spectroscopy, Chem. Soc. Rev. 46 (2017) 4042–4076, https://doi.org/10.1039/C7CS00238F.
[19] X. Yan, X. Shi, J. Ma, Fast quantification of the mixture of polycyclic aromatic hydrocarbons using surface-enhanced Raman spectroscopy combined with PLS-GA-BP network, J. Ocean Univ. China 20 (2021) 1451–1458, https://doi.org/10.1007/s11802-021-4832-y.
[20] X. Wang, N. Choi, Z. Cheng, J. Ko, L. Chen, J. Choo, Simultaneous detection of dual nucleic acids using a SERS-based lateral flow assay biosensor, Anal. Chem. 89 (2017) 1163–1169, https://doi.org/10.1021/acs.analchem.6b03536.
[21] M. Fan, G.F.S. Andrade, A.G. Brolo, A review on recent advances in the applications of surface-enhanced Raman scattering in analytical chemistry, Anal. Chim. Acta 1097 (2020) 1–29, https://doi.org/10.1016/j.aca.2019.11.049.
[22] R. Pan, Y. Yang, Y. Wang, S. Li, Z. Liu, Y. Su, B. Quan, Y. Li, C. Gu, J. Li, Nanocracking and metallization doubly defined large-scale 3D plasmonic sub-10 nm-gap arrays as extremely sensitive SERS substrates, Nanoscale 10 (2018) 3171–3180, https://doi.org/10.1039/C7NR08646F.
[23] C. Zhang, S.Z. Jiang, C. Yang, C.H. Li, Y.Y. Huo, X.Y. Liu, A.H. Liu, Q. Wei, S.S. Gao, X.G. Gao, B.Y. Man, Gold@silver bimetal nanoparticles/pyramidal silicon 3D substrate with high reproducibility for high-performance SERS, Sci. Rep. 6 (2016) 25243, https://doi.org/10.1038/srep25243. UK.
[24] P. Wang, O. Liang, W. Zhang, T. Schroeder, Y.H. Xie, Ultra-sensitive graphene-plasmonic hybrid platform for label-free detection, Adv. Mater. 25 (2013) 4918–4924, https://doi.org/10.1002/adma.201300635.
[25] A. Roy, A. Maiti, T.K. Chini, B. Satpati, Annealing induced morphology of silver nanoparticles on pyramidal silicon surface and their application to surface-enhanced raman scattering, ACS Appl. Mater. Interfaces 9 (2017) 34405–34415, https://doi.org/10.1021/acsami.7b08493.
[26] R.N. Cassar, D. Graham, I. Larmour, A.W. Wark, K. Faulds, Synthesis of size tunable monodispersed silver nanoparticles and the effect of size on SERS enhancement, Vib. Spectrosc. 71 (2014) 41–46, https://doi.org/10.1016/j.vibspec.2014.01.004.
[27] Q. Yang, J. Wang, H. Wu, S. Qin, J. Pan, C. Li, Hierarchically rough CuO/Ag composite film with controlled morphology as recyclable SERS-active substrate, Appl. Surf. Sci. 598 (2022), 153746, https://doi.org/10.1016/j.apsusc.2022.153746.
[28] H. Liang, Z. Li, W. Wang, Y. Wu, H. Xu, Highly surface-roughened "Flower-like" silver nanoparticles for extremely sensitive substrates of surface-enhanced Raman scattering, Adv. Mater. 21 (2009) 4614–4618, https://doi.org/10.1002/adma.200901139.
[29] J. Zeng, H. Jia, J. An, X. Han, W. Xu, B. Zhao, Y. Ozaki, Preparation and SERS study of triangular silver nanoparticle self-assembled films, J. Raman Spectrosc. 39 (2008) 1673–1678, https://doi.org/10.1002/jrs.2079.
[30] C. Liu, X. Xu, W. Hu, X. Yang, P. Zhou, G. Qiu, W. Ye, Y. Li, C. Jiang, Synthesis of clean cabbagelike (111) faceted silver crystals for efficient surface-enhanced Raman scattering sensing of papaverine, Anal. Chem. 90 (2018) 9805–9812, https://doi.org/10.1021/acs.analchem.8b01735.
[31] S. Xi, X. Zhang, Z. Luan, Z. Du, L. Li, Z. Liang, C. Lian, J. Yan, Micro-Raman study of thermal transformations of sulfide and oxysalt minerals based on the heat induced by laser. 9 (2019) 751.
[32] M. Khandelwal, A. Kumar, One-pot environmentally friendly amino acid mediated synthesis of N-doped graphene–silver nanocomposites with an enhanced multifunctional behavior, Dalton Trans. 45 (2016) 5180–5195, https://doi.org/10.1039/C5DT04880J.
[33] G. Lu, S. Mao, S. Park, R.S. Ruoff, J. Chen, Facile, noncovalent decoration of graphene oxide sheets with nanocrystals, Nano Res. 2 (2009) 192–200, https://doi.org/10.1007/s12274-009-9017-8.
[34] J.P. Camden, J.A. Dieringer, Y. Wang, D.J. Masiello, L.D. Marks, G.C. Schatz, R. P. Van Duyne, Probing the structure of single-molecule surface-enhanced Raman scattering hot spots, J. Am. Chem. Soc. 130 (2008) 12616–12617, https://doi.org/10.1021/ja8051427.
[35] A. Maity, A. Maiti, B. Satpati, A. Patsha, S. Dhara, T.K. Chini, Probing localized surface plasmons of trisoctahedral gold nanocrystals for surface enhanced Raman scattering, J. Phys. Chem. C 120 (2016) 27003–27012, https://doi.org/10.1021/acs.jpcc.6b09296.
[36] D. Lee, S. Yoon, Effect of nanogap curvature on SERS: a finite-difference time-domain study, J. Phys. Chem. C 120 (2016) 20642–20650, https://doi.org/10.1021/acs.jpcc.6b01453.
[37] L. Chen, B. Ying, P. Song, X. Liu, A nanocellulose-paper-based SERS multiwell plate with high sensitivity and high signal homogeneity, Adv. Mater. Interfaces 6 (2019), 1901346, https://doi.org/10.1002/admi.201901346.
[38] R.R. Juluri, A. Ghosh, A. Bhukta, R. Sathyavathi, P.V. Satyam, Silver endotaxy in silicon under various ambient conditions and their use as surface enhanced Raman spectroscopy substrates, Thin Solid Films 586 (2015) 88–94, https://doi.org/10.1016/j.tsf.2015.02.079.
[39] Y. Guo, J. Yu, C. Li, Z. Li, J. Pan, A. Liu, B. Man, T. Wu, X. Xiu, C. Zhang, SERS substrate based on the flexible hybrid of polydimethylsiloxane and silver colloid decorated with silver nanoparticles, Opt. Express 26 (2018) 21784–21796, https://doi.org/10.1364/OE.26.021784.
[40] H.K. Chin, P.Y. Lin, J. Chen, R. Kirankumar, Z.H. Wen, S. Hsieh, Polydopamine-mediated Ag and ZnO as an active and recyclable SERS substrate for rhodamine B with significantly improved enhancement factor and efficient photocatalytic degradation, Appl. Sci. 11 (2021) 4914, https://doi.org/10.3390/app11114914.
[41] X.G. Wang, J. Wang, Z.J. Jiang, D.W. Tao, X.Q. Zhang, C.W. Wang, Silver loaded anodic aluminum oxide dual-bandgap heterostructure photonic crystals and their application for surface enhanced Raman scattering, Appl. Surf. Sci. 544 (2021), 148881, https://doi.org/10.1016/j.apsusc.2020.148881.
[42] J. Wang, Y. Hu, X. Yu, X. Zhuang, Q. Wang, N. Jiang, J. Hu, Recyclable and ultrasensitive SERS sensing platform: deposition of atomically precise Ag152 nanoclusters on surface of plasmonic 3D ZnO-NC/AuNP arrays, Appl. Surf. Sci. 540 (2021), 148324, https://doi.org/10.1016/j.apsusc.2020.148324.
[43] D. Das, S. Senapati, K.K. Nanda, Rinse, repeat": an efficient and reusable SERS and catalytic platform fabricated by controlled deposition of silver nanoparticles on cellulose paper, ACS Sustain. Chem. Eng. 7 (2019) 14089–14101, https://doi.org/10.1021/acssuschemeng.9b02651.
[44] V.K. Rao, T.P. Radhakrishnan, Tuning the SERS response with Ag-Au nanoparticle-embedded polymer thin film substrates, ACS Appl. Mater. Interfaces 7 (2015) 12767–12773, https://doi.org/10.1021/acsami.5b04180.
[45] J.T.L. Navarrete, V. Hernández, F.J. Ramírez, Ir and Raman spectra of L-aspartic acid and isotopic derivatives, Biopolymers 34 (1994) 1065–1077, https://doi.org/10.1002/bip.360340810.